Radiofrequency Ablation for Small Hepatocellular Carcinoma:

Prospective Comparison of Internally Cooled Electrode and Expandable Electrode[1]

Toshiya Shibata, MD
Toyomichi Shibata, MD
Yoji Maetani, MD
Hiroyoshi Isoda, MD
Masahiro Hiraoka, MD

Purpose: To prospectively compare the effectiveness of radiofrequency (RF) ablation performed by using an internally cooled electrode and an expandable electrode for the treatment of small (≤3.0 cm) hepatocellular carcinomas (HCCs).

Materials and Methods: The human subjects research review board at the study institution approved the protocol, and each patient provided informed consent. Seventy-four patients (58 men and 16 women; age range, 41–83 years) with 83 HCC nodules 3 cm or smaller were randomly divided into an internally cooled electrode group (38 patients with 41 nodules) and an expandable electrode group (36 patients with 42 nodules). RF ablation was performed by one individual. Primary technique effectiveness and rates of major complications were evaluated between the two groups with the Fisher exact test. Rates of local tumor progression, overall survival, local progression–free survival, and event-free survival were evaluated by using the Kaplan-Meier method.

Results: The primary technique effectiveness was 95% in the internally cooled electrode group and 93% in the expandable electrode group (P = .51); rates of major complications were 0% and 2.1% per session (P = .50) and 0% and 2.8% per patient (P = .49), respectively. Rates at 1, 2, and 3 years in the internally cooled electrode group versus the expandable electrode group were as follows: local tumor progression, 12% versus 17%, 20% versus 22%, and 20% versus 22% (P = .72, log-rank test); overall survival, 100% versus 94%, 94% versus 92%, and 94% versus 77% (P = .29, log-rank test); local progression–free survival, 87% versus 78%, 73% versus 66%, and 73% versus 46% (P = .27, log-rank test); and event-free survival, 47% versus 44%, 34% versus 22%, and 34% versus 22% (P = .40, log-rank test).

Conclusion: On the basis of the study findings, RF ablation with an internally cooled electrode needle and an expandable electrode needle has equivalent effectiveness for the treatment of small HCCs.

---

[1] From the Department of Radiology, Kyoto University Graduate School of Medicine, 54-Kawaharacho, Shogoin, Sakyoku, Kyoto 606-8507, Japan. Received October 28, 2004; revision requested December 20; revision received March 3, 2005; final version accepted March 23.

Hepatocellular carcinoma (HCC) has gained major clinical interest because of its increasing worldwide incidence (1). Liver cancer is the fifth most common cancer in the world (564 000 cases per year) and the third most frequent cause of cancer-related death (2). Although surgical resection and liver transplantation are effective radical treatments, a small proportion of patients with HCC currently benefit from these treatments because of poor hepatic reserve or a shortage of donors (1). There are several nonsurgical options for the treatment of HCC, such as transcatheter arterial embolization, image-guided percutaneous ethanol injection, percutaneous acetic acid injection, percutaneous microwave coagulation, radiofrequency (RF) ablation, interstitial laser photocoagulation, and cryotherapy (3–13). Several reports have indicated that RF ablation is effective for the local control of small HCC nodules (7,10,11,14,15). The types of commercially available RF electrodes have been divided into three types: expandable electrode, internally cooled electrode, and saline-enhanced electrode (10,11,16); currently, expandable and internally cooled electrodes are widely used. Authors of some reports have compared the coagulation areas produced with commercially available RF devices in animal livers (17,18). To our knowledge, however, no single study has compared the effectiveness of the LeVeen (RadioTherapeutics, Mountain View, Calif) (hereafter, expandable electrode) and Cool-tip (Radionics, Burlington, Mass) (hereafter, internally cooled electrode) needles in humans. The purpose of our study, therefore, was to prospectively compare the effectiveness of RF ablation performed by using the internally cooled electrode and the expandable electrode for the treatment of small (≤3.0 cm) HCC nodules.

Materials and Methods

Patients

Between June 2001 and June 2003, 76 consecutive patients were referred to the department of radiology for RF ablation. Our criteria for RF ablation were three or fewer HCC nodules equal to or smaller than 3 cm in diameter. Of the 76 patients, two with an HCC nodule located near the colon refused RF ablation; one was treated with surgical resection and the other was treated with transcatheter arterial embolization. Seventy-four patients with 83 HCC nodules (58 men and 16 women; age range, 41–83 years; mean age ± standard deviation, 65.5 years ± 9.5) participated in this study. Of the 74 patients, 67 had a solitary nodule, five had two nodules, and two had three nodules. Nodule size ranged from 0.5 to 3.0 cm in diameter (mean, 1.9 cm ± 0.8). The human subjects research review board at our institution approved our protocol. Before treatment, informed consent was obtained from each patient. The patients were informed that according to the published literature, the RF technique with either the internally cooled electrode or the expandable electrode was effective for local control of HCC, and they were made aware of our study.

The patients were randomly assigned to undergo RF ablation with an internally cooled electrode or with an expandable electrode, according to a weekly schedule. RF ablation with the internally cooled electrode was performed every Tuesday (38 patients with 41 HCC nodules) and that with the expandable electrode (36 patients with 42 HCC nodules) was performed every Friday.

Imaging and Confirmation of Diagnosis

Pretreatment imaging studies performed were abdominal ultrasonography (US) and dynamic computed tomography (CT). Abdominal US was performed with a real-time scanner and a 3.5-MHz transducer (SSD-550; Aloka, Tokyo, Japan) by one author (Toyomichi Shibata) who did not know the patients' treatment group. Dynamic CT was performed with a helical CT scanner (HiSpeed Advantage; GE Medical Systems, Milwaukee, Wis). Triple-phase contiguous CT scans with 7-mm-thick sections were obtained. First, nonenhanced CT scans were obtained. Then, early-phase CT scans were obtained 30 seconds after the initiation of the bolus injection of 100 mL of 65% iopamidol (Iopamiron 300; Nihon Schering, Osaka, Japan); late-phase CT scans were obtained 120 seconds after the initiation of the injection of contrast media. One author (Y.M.), who did not know the patients' treatment group, diagnosed the CT findings. The European Association for the Study of the Liver (19) demonstrated that HCC can be diagnosed by means of coincident findings with at least two of three modalities—US, CT, or magnetic resonance imaging—that show characteristic features in a focal lesion. In our study, the diagnosis of HCC was obtained according to characteristic image findings at both US and dynamic CT in 55 of 74 patients; HCC was confirmed with percutaneous needle biopsy in the remaining 19 patients, who had nodules that could not be diagnosed as HCC according to the image findings.

RF Ablation

One author (Toshiya Shibata), who had 18 years of experience in interventional radiology, performed the RF ablation.

Internally cooled electrode.—The Cool-tip RF system, produced by Radionics, was used (9). The RF system consists of a 480-kHz generator; a 20- or 15-cm-long, 17-gauge cooled-tip RF electrode with a 2- to 3-cm-long ex-

Radiology 2006; 238:346–353

Abbreviations:
HCC = hepatocellular carcinoma
RF = radiofrequency

Author contributions:
Guarantor of integrity of entire study, Toshiya Shibata; study concepts/study design or data acquisition or data analysis/interpretation, all authors; manuscript drafting or manuscript revision for important intellectual content, all authors; approval of final version of submitted manuscript, all authors; literature research, Toshiya Shibata, Y.M., H.I., M.H.; clinical studies, Toshiya Shibata, Toyomichi Shibata; experimental studies, H.I.; statistical analysis, Toshiya Shibata, Y.M.; and manuscript editing, Toshiya Shibata, Toyomichi Shibata, M.H.

Address correspondence to Toshiya Shibata
(e-mail: *ksj@kuhp.kyoto-u.ac.jp*).

posed metallic tip; and a dispersive pad applied to the patient's skin. Grounding was achieved by attaching a dispersive pad to each of the patient's thighs. Pentazocine (15 mg, Sosegon; Yamanouchi Pharmaceutical, Tokyo, Japan) was intramuscularly injected 10 minutes before therapy as premedication for sedation. After the skin surface was disinfected, induction of local anesthesia with 1% lidocaine (Xylocaine; AstraZeneca, Osaka, Japan) was performed.

For nodules that were up to 1.5 cm in diameter, an electrode with a 2-cm exposed metallic tip was introduced into the center of the nodules by using either US or CT guidance. An electrode with a 3-cm exposed metallic tip was introduced into the center of nodules that were 1.5–2.5 cm in diameter. For nodules greater than 2.5 cm in diameter, a multiple electrode insertion technique was applied. Two electrodes with a 3-cm exposed metallic tip were inserted in the peripheral parts of the tumor, with an interelectrode distance of 1.5–2.0 cm.

During RF ablation, a thermocouple embedded in the electrode tip continuously measured the local temperature. Tissue impedance was monitored continuously by means of circuitry incorporated in the generator. A peristaltic pump (Watson-Marlow, Wilmington, Mass) was used to infuse 0°C normal saline solution into the cooling lumen of the electrode at a rate sufficient to maintain a tip temperature of 20°C–25°C. RF energy was delivered in the following manner: After measurement of baseline tissue impedance, generator output was slowly increased to 1000–1400 mA, and this level was maintained until the end of the procedure. If an increase in impedance equal to or greater than 10 above baseline was observed, the current was reduced until stable impedance was observed and then increased again. The process of decreasing and increasing generator output was repeated for the remainder of the treatment session to prevent tissue charring, which leads to increased impedance and limited energy deposition. The length of these cycles of increased and decreased generator output varied according to tissue impedance; in general, however, decreased output was maintained for approximately 15 seconds. An analgesic (pentazocine, 15 mg) was administered intravenously for patients who experienced severe pain during or immediately after the treatments.

Expandable electrode.—The RF 2000 generator system, produced by RadioTherapeutics, was used (10). This system consists of a generator, a monopolar array needle electrode (LeVeen), and a dispersive electrode pad applied to the patient's skin. The RF generator has a 460-kHz frequency and features displays indicating tissue impedance value and procedure time. The needle electrode is a 15-gauge insulated cannula with eight or 10 expandable hook-shaped electrode tines, whose diameters are 2.0 or 3.0 cm at expansion. Grounding was achieved by attaching a dispersive pad to each of the patient's thighs. Pentazocine (15 mg) was intramuscularly injected 10 minutes before therapy as premedication for sedation. After the skin surface was disinfected, induction of local anesthesia with 1% lidocaine was performed.

For nodules up to 1.5 cm in diameter, an electrode with 2.0-cm expanded tines, which was connected to the RF generator with a soft cable, was introduced into the center of the nodules by using either US or CT guidance. Hooks were then deployed in situ in the nodule. An initial power of 30 W was applied and increased at a rate of 10 W/min to 90 W. RF energy was applied until either marked increases in impedance were achieved or 15 minutes had elapsed. The second treatment was then applied at the same position until either marked increases in impedance were achieved or 10 minutes had elapsed at the 75% of the maximum output of the first treatment. If the marked increases in impedance were not obtained after the second treatment within 10 minutes, the third treatment was initiated at the same power of the second treatment and increased at a rate of 10 W/min to 90 W maximum, until marked increases in impedance were obtained. During procedures, an analgesic (pentazocine, 15 mg) was administered intravenously for patients who experienced severe pain during or immediately after the treatments.

For nodules 1.5–2.5 cm in diameter, an electrode with 3.0-cm expanded tines was introduced into the center by using US guidance. An initial power of 40 W was applied and increased at a rate of 10 W/min to 90 W. RF energy was applied until either marked increases in impedance were achieved or 15 minutes had elapsed. The second treatment was then applied at the same position until either marked increases in impedance were achieved or 10 minutes had elapsed at the 75% of the maximum output of the first treatment. If the marked increases in impedance were not obtained after the second treatment during 10 minutes, the third treatment was initiated at the same power of the second treatment and increased at a rate of 10 W/min to 90 W maximum, until marked increases in impedance were obtained. During procedures, an analgesic (pentazocine, 15 mg) was administered intravenously for patients who experienced severe pain during or immediately after the treatments.

For nodules larger than 2.5 cm in diameter, a multiple-electrode insertion technique was applied. Two electrodes were inserted in the peripheral parts of the tumor, with an interelectrode distance of 1.5–2.0 cm. The electrode used in the multiple-electrode insertion technique was the same as that used with the 3.0-cm expanded tines.

Treatment Course and Follow-up

Treatment course.—One to 2 days after each treatment session, dynamic CT was performed with the same protocols as the pretreatment imaging studies to diagnose the spread of the coagulation areas. One author (Y.M.) evaluated the CT findings. When a nonenhancing area with a diameter greater than that of the treated nodule was depicted, the treatment was finished. When nodule enhancement was seen at dynamic CT, an additional RF treatment was performed for the residual enhanced lesion. We limited the total number of treatment sessions for each nodule to no more than three so that a treatment course included one to three RF sessions. The effectiveness of the RF ablation technique was evaluated with dynamic CT performed 3–4 weeks after the first RF ablation session was performed. When no enhancing lesion was seen at CT, the technique effectiveness was defined as complete. When nodule enhancement was still seen at CT, the technique effectiveness was defined as incomplete (19). The nodules showing incomplete technique effectiveness were not treated with additional RF ablation but rather with transcatheter arterial embolization. Primary technique effectiveness rates (19) were evaluated in our study.

Follow-up US and dynamic CT were performed at 3-month intervals with the same protocols as the pretreatment studies. Local tumor progression was defined as a newly appearing enhancing lesion in or near the treated nodule at dynamic CT (19). The occurrence of new lesions in the liver and tumor dissemination or tumor implantation along the electrode tract were evaluated with US and dynamic CT. One author (Toyomichi Shibata) performed US, and another author (Y.M.) assessed the dynamic CT findings. Follow-up periods after RF ablation were 10–41 months (mean, 27 months ± 6.8) overall, 10–41 months (mean, 28 months ± 7.9) in the expandable electrode group, and 16–40 months (mean, 21 months ± 5.7) in the internally cooled electrode group.

Comparison.—The following points were compared between the internally cooled electrode and expandable electrode groups:

1. Rates of primary technique effectiveness in each nodule.

2. Rates of major complications: In accordance with the complication definitions established by the Society of Interventional Radiology, specific complications of interventional procedures were assigned to major and minor categories (20). Major complications were defined as those that required therapy with hospitalization or involved permanent adverse sequelae, including death. Major complications occurring after percutaneous ablation therapy for liver tumors are hemorrhage requiring transfusion, liver abscess requiring percutaneous drainage, bile duct injury requiring biliary drainage, pleural effusion requiring thoracentesis, tumor dissemination, hepatic failure, and death. Each one of two authors (H.I. and M.H.) assessed the major complications.

3. Rates of local tumor progression in each nodule: The time from the beginning of RF ablation to last follow-up CT was used.

4. Rates of overall survival: The time from the beginning of RF ablation to last follow-up CT or death was used.

5. Rates of local tumor progression–free survival: The time from the beginning of RF ablation to last follow-up CT, local tumor progression, or death was used.

6. Rates of event-free survival: The time from the beginning of RF ablation to last follow-up CT, local tumor progression, occurrence of new lesions in the liver, distant metastasis, or death was used.

Statistical Analysis

The variables in the internally cooled electrode and expandable electrode groups were compared. Patient age and size of nodules were statistically evaluated by using the Student *t* test. Patient sex, positivity for hepatitis C virus antibody, positivity for hepatitis B surface antigen, and serum α-fetoprotein level greater than 200 μg/L were evaluated by using χ^2 analysis. Number of nodules and Child-Pugh classification were evaluated by using the Wilcoxon test. Rates of primary technique effectiveness and of major complications were evaluated by using the Fisher exact test. Rates of local tumor progression, overall survival, local tumor progression–free survival, and event-free survival were estimated by using the Kaplan–Meier method. We compared these rates between the two groups by performing the log-rank test. Prognostic value of baseline characteristics, such as patient age and sex, Child-Pugh class, positivity for hepatitis C virus antibody, positivity for hepatitis B surface antigen, serum α-fetoprotein level greater than 200 μg/L, and number and size of nodules, was assessed by using Cox proportional hazards regression models. A P value $< .05$ was considered to indicate a significant difference. Data processing and analysis were performed by using commercially available software (SPSS for Windows, version 9.0; SPSS, Chicago, Ill).

Results

No significant differences were observed between the internally cooled electrode and expandable electrode groups with respect to the following baseline characteristics: patient age and sex; Child-Pugh class; proportions of patients positive for hepatitis C virus antibody, positive for hepatitis B surface antigen, and with elevated serum α-fetoprotein levels; number of nodules; or size of nodules (Table).

Sessions

A total of 95 sessions of RF ablation were performed for 74 patients with 83 HCC nodules. Of 48 sessions performed with the internally cooled electrode needle, a single treatment session was performed in 31 patients, two sessions were performed in four patients, and three sessions were performed in three patients. Of 47 sessions performed with the expandable electrode needle, a single treatment session was performed in 27 patients, two sessions were performed in seven patients, and three sessions were performed in two patients. In 43 (91%) of 47 sessions, the sudden increase in impedance and reduction in the current (roll-off) were observed.

Primary Technique Effectiveness

In the internally cooled electrode group of 41 nodules, 39 (95%) showed complete technique effectiveness and two (4.9%) had incomplete technique effectiveness; these two were deeply located in the caudate lobe. In the expandable electrode group of 42 nodules, 39 (93%) showed complete technique effectiveness and three (7.1%) showed incomplete technique effectiveness; two of these three were located near the hepatic veins and inferior vena cava.

There was no significant difference with respect to the rates of primary technique effectiveness between the two groups (*P* = .51, Fisher exact test).

Major Complications

A major complication—tumor implantation along the electrode tract—occurred with one session (2.1% per session) in one patient (2.8% per patient) in the expandable electrode group. No major complication occurred in the internally cooled electrode group. There was no significant difference in the rates of major complications between the two groups (*P* = .50 for difference according to session and *P* = .49 for difference according to patient, Fisher exact test).

Local Tumor Progression Rates

During follow-up, local tumor progression developed in eight nodules in the internally cooled electrode group and in nine nodules in the expandable electrode group. Of the nodules with local tumor progression, one nodule in the internally cooled electrode group and three nodules in the expandable electrode group were located near the inferior vena cava and hepatic veins (Fig 1). Two nodules in the internally cooled electrode group were deeply located in the caudate lobe. According to the Kaplan-Meier method, local tumor progression rates (Fig 2) in the internally cooled electrode group versus the expandable electrode group at 1, 2, and 3 years were as follows: 12% versus 17%, 20% versus 22%, and 20% versus 22%. There was no significant difference in the rates of local tumor progression between the two groups (*P* = .72, log-rank test).

Overall Survival Rates

During follow-up (Fig 3), two patients in the internally cooled electrode group died of multiple tumor progression in the liver. Five patients in the expandable electrode group died: three of multiple tumor progression in the liver, one of multiple tumor progression in the liver and lung, and one of cerebral hemorrhage. The overall survival rates in the internally cooled electrode group versus the expandable electrode group at 1, 2, and 3 years were 100% versus 94%, 94% versus 92%, and 94% versus 77%. There was no significant difference in the overall survival rates between the two groups (*P* = .29, log-rank test).

Rates of Local Tumor Progression–free Survival

The rates of local progression-free survival (Fig 4) in the internally cooled electrode group versus the expandable electrode group at 1, 2, and 3 years were 87% versus 78%, 73% versus 66%, and 73% versus 46%. No significant difference was observed between the two groups (*P* = .27, log-rank test).

Event-free Survival Rates

The event-free survival rates in the internally cooled electrode group versus the expandable electrode group at 1, 2, and 3 years were 47% versus 44%, 34% versus 22%, and 34% versus 22%. No significant difference was observed between the two groups (*P* = .40, log-rank test).

By using Cox proportional hazards model, baseline variables (patient age and sex, Child-Pugh class, positivity for hepatitis C virus antibody, positivity for hepatitis B surface antigen, serum α-fetoprotein level >200 μg/L, and number and size of nodules) were not prognostically relevant with respect to the rates of overall survival, local tumor progression-free survival, and event-free survival.

Discussion

Of several ablation therapies for HCC, such as percutaneous ethanol injection, percutaneous acetic acid injection, percutaneous microwave coagulation, RF ablation, interstitial laser photocoagulation, and cryosurgery, percutaneous ethanol injection has been a standard treatment option and has been widely performed because of its safety, low cost, and effectiveness (21). Findings of recent studies, however, have shown that RF ablation is superior to percutaneous ethanol injection with regard to achievement of complete tumor response or local recurrence-free survival rates (14,15). It has been demonstrated that RF tumor ablation could be achieved with fewer sessions than percutaneous microwave coagulation (7). Although, to our knowledge, no reports have compared the effectiveness of RF ablation with that of interstitial laser photocoagulation or cryosurgery, RF ablation has been more widely performed than interstitial laser photocoagulation or cryosurgery and currently is one of the most effective ablation treatments for small HCC.

With RF ablation, local control of tumors is very important for achieving

Baseline Characteristics of 74 Patients Treated with RF Ablation

Characteristic	Internally Cooled Electrode Group (*n* = 38)	Expandable Electrode Group (*n* = 36)	*P* Value
Mean age (y)*	66.1 ± 9.4 (41–78)	65.0 ± 9.6 (44–83)	.60
No. of men/women	29/9	29/7	.66
Child-Pugh class†			
A	29	26	.69
B	9	10	
C	0	0	
Positivity for hepatitis C virus†	28	26	.89
Positivity for HBsAg†	6	6	.92
Serum AFP > 200 μg/L†	7	10	.34
No. of nodules	41	42	.22
Mean size (mm)*	17.5 ± 6.8 (5–30)	19.7 ± 8.4 (8–30)	.19

* Data are the mean ± standard deviation, data in parentheses are the range.

† Data are the number of patients. AFP = α-fetoprotein, HBsAg = hepatitis B surface antigen.

good patient survival, and successful tumor ablation is achieved when the tumor is completely destroyed by heat. The ideal for RF ablation would be to create a larger coagulation area than the tumor area during one session. Currently, three main strategies have been developed to enlarge coagulation areas: perfusion, internally cooled straight electrodes, and multitined expandable electrodes. De Baere et al (17) reported that the internally cooled cluster electrode clearly induced significantly larger lesions than the expandable needle in explanted calf livers ($P < .002$) and in vivo in swine livers ($P < .001$). They discussed the higher delivery of power exceeding 100 W (up to 200 W) in the Cool-tip system and attributed it to a larger coagulation area than that obtained with the expandable electrode, in which the maximum power delivered was up to 50 W (model 500; RITA Medical Systems, Mountain View, Calif). Pereira et al (18) compared four commercially available devices (perfusion, internally cooled cluster, and nine- and 12-tine expandable electrodes) in pig livers and showed that the maximum coagulation volumes were obtained with the perfusion electrode, followed by the internally cooled cluster, the 12-tine expandable electrode, and the nine-tine expandable electrode. However, they reported that high power output was not of primary importance for obtaining large coagulation volumes because excessive power output leads to overheating and tissue desiccation.

In our study, the rates of complete technique effectiveness evaluated at early-stage CT after RF ablation were comparatively high in both the internally cooled electrode and expandable electrode groups at 95% and 93%, respectively. For small HCC nodules no greater than 3 cm, sufficient coagulation areas would be obtained with the expandable electrode, as well as with the internally cooled electrode. Although the Cool-tip system has high delivery up to 200 W, the maximum power used for each treated nodule was 80–130 W in our study. The delivery of power greater than 130 W induced a frequent increase in impedance and multiple automatic reduction of the current that might consequently diminish the total treated times. On the other hand, the newly designed RF 3000 system (RadioTherapeutics), with multitine expandable electrode needle, can deliver power up to 200 W, but we believe that delivery of higher power up to 200 W, when electrodes with 2.0- or 3.0-cm expanded tines are used, may induce tissue charring around the electrode. Arata et al (22) reported that roll-off—the sudden increase of impedance and reduction in the current—is a significant predictor of local control after RF ablation because the local recurrence rate of the liver tumors treated with expandable electrode needle was 43% without roll-off and 15% with roll-off ($P = .024$). In our study, roll-off was obtained in most nodules (43 of 47 [91.5%]) in the expandable electrode group by using maximum 90-W power of the RF generator 2000 system.

Even if apparent coagulation necrosis were noted at early-stage dynamic CT, residual microscopic nests of tumor would lead to local tumor progression in some patients. Several causes have been suggested for the unsatisfactory results: technical difficulties in localizing the tumor and accurately placing the ablation electrode, heterogeneous thermodynamic properties of tissue in the ablation field (eg, the heat-sink effects of blood vessels in close proximity), and the different volume and geometry of

Figure 1

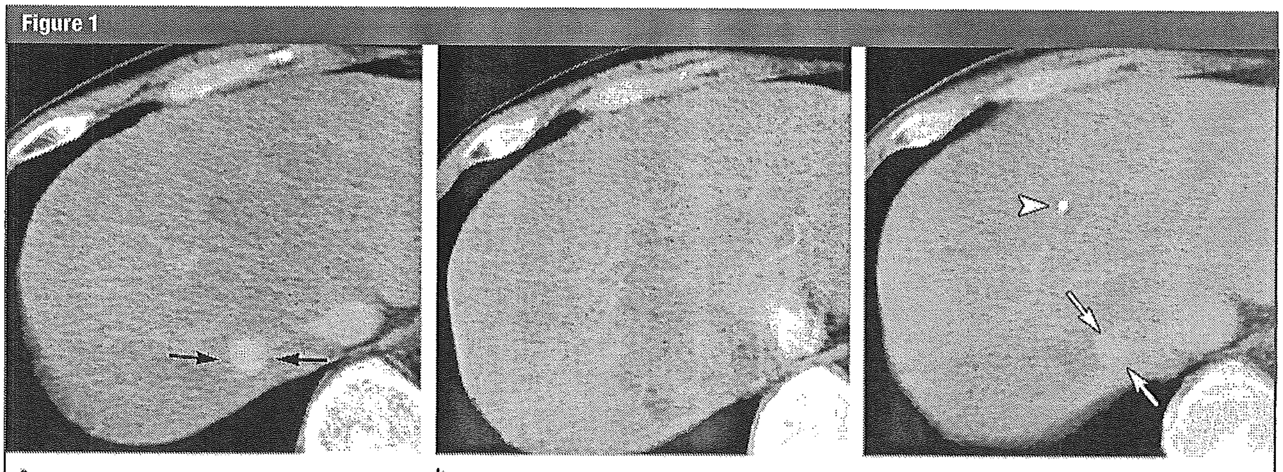

Figure 1: Early-phase transverse CT scans of an HCC nodule located near the right hepatic vein in a 73-year-old man. The nodule was treated with RF ablation and an internally cooled electrode needle. Intrahepatic metastatic nodules were diagnosed 10 months after RF ablation and were treated with transcatheter arterial embolization. Local tumor progression was diagnosed 17 months after RF ablation. **(a)** Scan obtained before RF ablation shows a 1.9-cm enhancing tumor (arrows) in the right posterosuperior segment. **(b)** Scan obtained 3 weeks after RF ablation shows no enhancement in the tumor area. The technique effectiveness was considered complete. **(c)** Scan obtained 17 months after RF ablation shows local tumor progression (arrows) just near the treated area. Iodized oil injected at the site of previous transcatheter arterial embolization is accumulated in an HCC nodule (arrowhead).

Figures 2–4

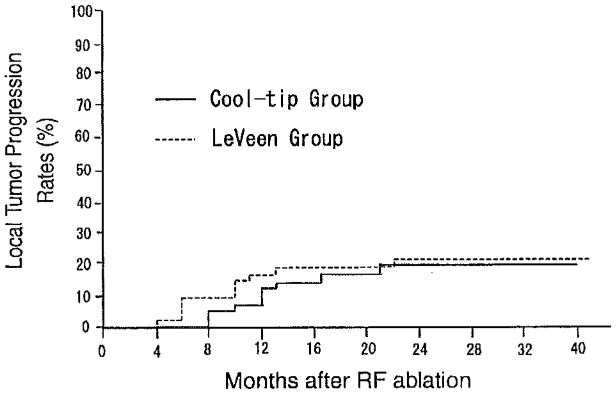

2.

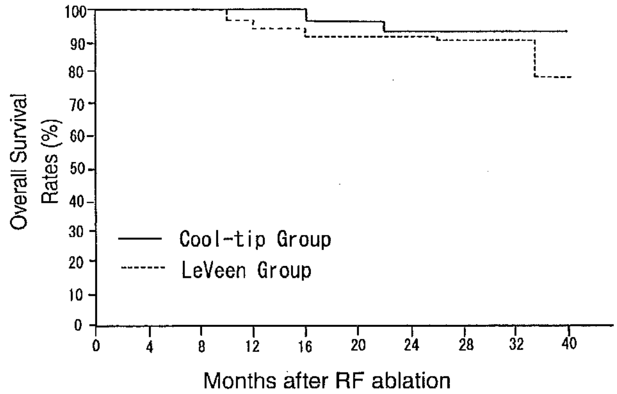

3.

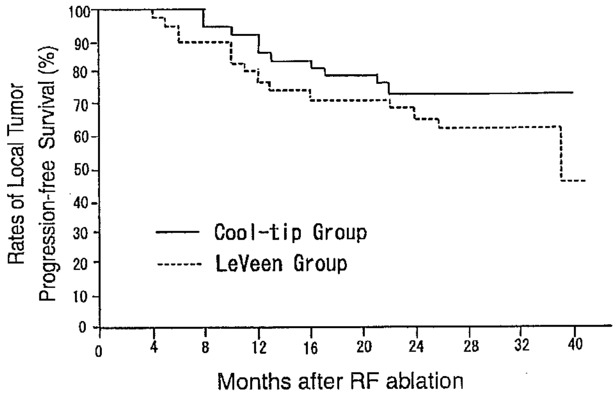

4.

Figure 2: Graph shows rates of local tumor progression in HCC nodules treated with internally cooled electrode *(Cool-tip)* needle ($n = 41$) or expandable electrode *(LeVeen)* needle ($n = 42$). No significant difference was noted between the two groups ($P = .72$, log-rank test).

Figure 3: Graph shows overall survival rates in patients with small HCC nodules treated with internally cooled electrode *(Cool-tip)* needle ($n = 38$) or expandable electrode *(LeVeen)* needle ($n = 36$). No significant difference was noted between the two groups ($P = .29$, log-rank test).

Figure 4: Graph shows local progression–free survival rates in patients with small HCC nodules treated with internally cooled electrode *(Cool-tip)* needle ($n = 38$) or expandable electrode *(LeVeen)* needle ($n = 36$). No significant difference was noted between the two groups ($P = .27$, log-rank test).

ablation achieved with different ablation devices (23). Rates of local tumor progression after RF ablation of HCC or metastatic liver tumor have been reported to vary from 1.8% to 34%–55% (10–11,24–26). In our study, the rates of local tumor progression of the internally cooled electrode group versus the expandable electrode group at 1, 2, and 3 years were 12% versus 17%, 20% versus 22%, and 20% versus 22% ($P = .72$). Although our rates of local tumor progression are not low, heat-sink effects would affect the unsatisfactory results in four nodules located near the inferior vena cava and hepatic veins (three in the expandable electrode group and one in the internally cooled electrode group), and difficulty in accurately placing the ablation electrode affected the results in two nodules in the internally cooled electrode group located in the caudate lobe.

No significant difference was noted between the two groups with regard to local tumor progression ($P = .72$) or tumor progression–free survival rates ($P = .27$). RF ablation with the two different electrodes showed the equivalent effectiveness of local control of small HCC. So, which electrode should we choose? With US guidance, precise depiction of the tip of the expanded tines may not be clear in some cases. We believe the expandable electrode should not be used for nodules just near the heart or gastrointestinal tract to avoid direct injury of the organs. The shape of the coagulation area produced with the expandable electrode has been more oval than that produced with the perfusion or internally cooled electrode (18). When the nodule's short axis vertical to the inserted electrode is long, we should choose an expandable electrode. Major complications rarely occurred: Rates were 0% in the internally cooled electrode group and 2.1% per session and 2.8% per patient in the expandable electrode group. We believe both RF techniques proved to be equally a safe technique.

Our study had some limitations in that RF ablation is currently undergoing major modifications so that newer techniques or refined treatment strategies may produce larger areas of tumor coagulation and result in better local tumor response rates. In our study, long-term follow-up was needed to compare the local control of tumor or patient survival between the internally cooled electrode and expandable electrode groups, and the RF generator with expandable electrode used in our study has been replaced by a newer device with higher power output (RF 3000 system).

In conclusion, the two RF ablation devices used in our study have equivalent primary technique effectiveness, rates of major complications, rates of local tumor progression, rates of overall survival, and rates of local tumor progression–free survival.

References

1. El-Serag HB, Mason AC. Rising incidence of hepatocellular carcinoma in the United States. N Engl J Med 1999;340:745–750.
2. Parkin DM, Bray F, Ferlay J, et al. Estimating the world cancer burden: GLOBOCAN 2000. Int J Cancer 2001;94:153–156.
3. Llovet JM, Bruix J. Systematic review of randomized trials for unresectable hepatocellular carcinoma: chemoembolization improves survival. Hepatology 2003;37:429–442.
4. Kotoh K, Sakai H, Sakamoto S, et al. The effect of percutaneous ethanol injection therapy on small solitary hepatocellular carcinoma is comparable to that of hepatectomy. Am J Gastroenterol 1994;89:194–198.
5. Livraghi T, Giorgio A, Marin G, et al. Hepatocellular carcinoma and cirrhosis in 746 patients: long-term results of percutaneous ethanol injection. Radiology 1995;197:101–108.
6. Ohnishi K, Yoshioka H, Ito S, et al. Prospective randomized controlled trial comparing percutaneous acetic acid injection and percutaneous ethanol injection for small hepatocellular carcinoma. Hepatology 1998;27:67–72.
7. Shibata T, Iimuro Y, Yamamoto Y, et al. Small hepatocellular carcinoma: comparison of radio-frequency ablation and percutaneous microwave coagulation therapy. Radiology 2002;223:331–337.
8. Lu MD, Chen JW, Xie XY, et al. Hepatocellular carcinoma: US-guided percutaneous microwave coagulation therapy. Radiology 2001;221:167–172.
9. Solbiati L, Goldberg SN, Ierace T, et al. Hepatic metastasis: percutaneous radio-frequency ablation with cooled-tip electrodes. Radiology 1997;205:367–373.
10. Curley SA, Izzo F, Ellis L, et al. Radiofrequency ablation of hepatocellular cancer in 110 patients with cirrhosis. Ann Surg 2000; 232:381–391.
11. Goldberg SN, Gazelle GS, Mueller PR. Thermal ablation therapy for focal malignancies: a unified approach to underlying principles, techniques, and diagnostic imaging guidance. AJR Am J Roentgenol 2000;174:323–331.
12. Vogl TJ, Mack MG, Roggan A, et al. Internally cooled power laser for MR-guided interstitial laser-induced thermotherapy of liver lesions: initial clinical results. Radiology 1998;209:381–385.
13. Huang A, McCall JM, Weston MD, et al. Phase I study of percutaneous cryotherapy for colorectal liver metastasis. Br J Surg 2002;89:303–310.
14. Livraghi T, Goldberg SN, Lazzaroni S, et al. Small hepatocellular carcinoma: treatment with radio-frequency ablation versus ethanol injection. Radiology 1999;210:655–661.
15. Lencioni RA, Allgaier HP, Cioni D, et al. Small hepatocellular carcinoma in cirrhosis: randomized comparison of radio-frequency thermal ablation versus percutaneous ethanol injection. Radiology 2003;228:235–240.
16. Giorgio A, Tarantino L, de Stefano G, et al. Percutaneous sonographically guided saline-enhanced radiofrequency ablation of hepatocellular carcinoma. AJR Am J Roentgenol 2003;181:479–484.
17. de Baere T, Denys A, Wood BJ, et al. Radiofrequency liver ablation: experimental comparative study of water-cooled versus expandable systems. AJR Am J Roentgenol 2001;176:187–192.
18. Pereira PL, Trubenbach J, Schenk M, et al. Radiofrequency ablation: in vivo comparison of four commercially available devices in pig livers. Radiology 2004;232:482–490.
19. Goldberg SN, Charboneau JW, Dodd GD 3rd, et al. Image-guided tumor ablation: proposal for standardization of terms and reporting criteria. Radiology 2003;228:335–345.
20. Leoni CJ, Potter JE, Rosen MP, et al. Classifying complications of interventional procedures: a survey of practicing radiologists. J Vasc Interv Radiol 2001;12:55–59.
21. Bruix J, Sherman M, Llovet JM, et al. Clinical management of hepatocellular carcinoma: conclusions of the Barcelona-2000 EASL conference. European Association for the Study of the Liver. J Hepatol 2001;35:421–430.
22. Arata MA, Nisenbaum HL, Clark TW, Soulen MC. Percutaneous radiofrequency ablation of liver tumors with the LeVeen probe: is roll-off predictive of response? J Vasc Interv Radiol 2001;12:455–458.
23. Dodd GD 3rd, Frank MS, Aribandi M, Chopra S, Chintapalli KN. Radiofrequency thermal ablation: computer analysis of the size of the thermal injury created by overlapping ablations. AJR Am J Roentgenol 2001;177: 777–782.
24. Solbiati L, Ierace T, Goldberg SN, Sironi S, Livraghi T, Fiocca R. Percutaneous US-guided radio-frequency tissue ablation of liver metastases: treatment and follow-up in 16 patients. Radiology 1997;202:195–203.
25. Kainuma O, Asano T, Aoyama H, et al. Combined therapy with radiofrequency thermal ablation and intra-arterial infusion chemotherapy for hepatic metastases from colorectal cancer. Hepatogastroenterology 1999;46: 1071–1077.
26. Livraghi T, Goldberg SN, Lazzaroni S, Meloni F, Ierace T, Solbiati L. Hepatocellular carcinoma: radio-frequency ablation of medium and large lesions. Radiology 2000;214: 761–768.

Diffusion-Tensor Fiber Tractography: Intraindividual Comparison of 3.0-T and 1.5-T MR Imaging[1]

Tsutomu Okada, MD
Yukio Miki, MD, PhD
Yasutaka Fushimi, MD
Takashi Hanakawa, MD, PhD
Mitsunori Kanagaki, MD, PhD
Akira Yamamoto, MD
Shin-ichi Urayama, PhD
Hidenao Fukuyama, MD, PhD
Masahiro Hiraoka, MD, PhD
Kaori Togashi, MD, PhD

Purpose: To prospectively evaluate the depiction of brain fiber tracts at 3.0- versus 1.5-T diffusion-tensor (DT) fiber tractography performed with parallel imaging.

Materials and Methods: Institutional review board approval was obtained, and each subject provided written informed consent. Subjects were 30 healthy volunteers (15 men, 15 women; mean age, 28 years; age range, 21–46 years). Single-shot spin-echo echo-planar magnetic resonance (MR) sequences with parallel imaging were applied. Four fiber tracts were reconstructed: corticospinal tract (CST), superior longitudinal fasciculus (SLF), corpus callosum (CC), and fornix. Two neuroradiologists compared 3.0- and 1.5-T tractography in terms of fiber tract depiction by using five depiction scores (scores 0–4) and numbers of reconstructed tract fibers and in terms of lateral asymmetry in the CST by using numbers of reconstructed fibers. The Wilcoxon signed rank test was applied for statistical analysis.

Results: Visual scores for both CST hemispheres ($P < .001$), the right SLF ($P = .005$), the CC ($P = .01$), and the right fornix ($P = .04$) were higher at 3.0-T DT tractography. Larger numbers of CST (right, $P = .008$; left, $P < .001$), SLF (right, $P = .001$; left, $P = .02$), and fornix (bilaterally, $P = .02$) tract fibers were depicted at 3.0 T. The asymmetry index for the CST was lower ($P < .001$) at 3.0 T. Visual scores for the left SLF and the left fornix and numbers of CC tract fibers were not significantly different.

Conclusion: Depiction of most fiber tracts was improved at 3.0-T DT tractography compared with depiction at 1.5-T tractography.

---

[1] From the Department of Diagnostic Imaging and Nuclear Medicine (T.O., Y.M., Y.F., M.K., A.Y., K.T.) and Department of Therapeutic Radiology and Oncology (M.H.), Graduate School of Medicine, and Human Brain Research Center (T.H., S.U., H.F.), Kyoto University, 54 Kawahara-cho, Shogoin, Sakyo-ku, Kyoto-shi, Kyoto 606-8507, Japan. From the 2004 RSNA Annual Meeting. Received December 30, 2004; revision requested March 17, 2005; revision received May 4; final version accepted June 1. Supported in part by grants from the Ministry of Health, Labor and Welfare of Japan (k0800006-01) and the Ministry of Education Culture, Sports, Science and Technology of Japan (C)(15591270).

Diffusion-tensor (DT) imaging is a magnetic resonance (MR) imaging technique that is sensitive to the orientation of mobility in intravoxel water molecules (1,2). DT imaging reveals two specific characteristics: diffusion anisotropy and the directional distribution of water diffusivity. When water diffusion in a tissue is almost the same in all directions, the diffusion is considered to be isotropic and have lower anisotropy. Conversely, when water diffusion is restricted along a specific direction, the diffusion is considered to be anisotropic and have higher anisotropy. Brain white matter has high diffusion anisotropy because diffusion is faster when it is parallel to the fiber direction than when it is the same in all other directions (3,4).

DT images of the human brain can be reconstructed for visualization of the macroscopic three-dimensional fiber tract architecture by using a process known as fiber tractography, or the fiber-tracking technique (5–10). DT imaging and fiber tractography are powerful tools for studying cerebral white matter and have been applied clinically to assess brain tumors (11,12), diffuse axonal injury (13), pediatric brain development (14), and cerebral infarcts (15).

With recent advances in actively shielded 3.0-T magnets, the use of high-field-strength MR imaging in clinical settings has become practical (16,17). Parallel imaging techniques, such as simultaneous acquisition of spatial harmonics, or SMASH (18); sensitivity encoding (19); and auto-SMASH–based generalized autocalibrating partially parallel acquisition (20), also have improved with recent advances in MR imaging hardware. Owing to shortened echo train lengths and echo times, parallel imaging techniques can be used to reduce artifacts related to spin-echo echo-planar imaging. Some reports have described the performance of parallel imaging in spin-echo echo-planar DT imaging and fiber tractography at 1.5 or 3.0 T (9,10,21–24). However, to our knowledge, in no reports have the differences between 3.0- and 1.5-T spin-echo echo-planar DT fiber tractography with parallel imaging been compared. Thus, the purpose of our study was to prospectively evaluate the depiction of brain fiber tracts at 3.0-T versus 1.5-T DT fiber tractography performed with parallel imaging.

Materials and Methods

Study Subjects

The study population comprised 30 healthy volunteers (15 men, 15 women; mean age, 28 years; age range, 21–46 years) with no history of neurologic injury or psychiatric disease. All subjects were examined by one of the authors (T.H., with 14 years of experience as a neurologist), and no subjects had abnormal neurologic signs or symptoms. Institutional review board approval was obtained for this study, and each subject provided written informed consent.

Data Acquisition

All subjects underwent 3.0- and 1.5-T DT imaging, which was performed by using a whole-body 3.0-T MR unit (Trio; Siemens, Erlangen, Germany) with a 40 mT/m gradient and a 1.5-T MR unit (Symphony; Siemens) with a 30 mT/m gradient, on the same day. MR imaging at 3.0 T was performed by one author (T.O.), and MR imaging at 1.5 T was performed by another author (Y.F.), both of whom had 8 years of experience as neuroradiologists and 2 years of experience in DT imaging. The time delay between 3.0- and 1.5-T MR imaging was less than 1 hour for all subjects. Both MR units were equipped with integrated parallel acquisition capability and a receive-only eight-channel phased-array head coil. Both the 3.0-T and the 1.5-T DT imaging examinations involved the use of single-shot spin-echo echo-planar sequences and nearly identical parameters: 5200/79 (repetition time msec/echo time msec), a 220-mm field of view, a 128 × 128 matrix, 3-mm section thickness without intersection gaps (matrix size, 1.7 × 1.7 × 3.0 mm), and four repetitions.

The generalized autocalibrating partially parallel acquisition algorithm was applied for parallel imaging with use of a reduction factor of two, 24 additional autocalibrating phase-encoding steps in the center of k-space, and a 75% partial Fourier technique in the phase-encoding direction. Only the bandwidths differed: A bandwidth of 1502 Hz per pixel was used for 3.0-T imaging, and a bandwidth of 1056 Hz per pixel was used for 1.5-T imaging. Motion-probing gradients were applied along 12 noncolinear directions with a b factor of 700 sec/mm^2 after one non–diffusion-weighted image (b = 0 sec/mm^2) was obtained. A total of 40 sections encompassed the entire cerebral hemisphere and the brainstem. The imaging times for 3.0- and 1.5-T DT imaging were almost the same—about 7.5 minutes.

Data Processing

DT imaging data sets were transferred, in Digital Imaging and Communications in Medicine format, to a Windows personal computer (IBM, New York, NY) workstation. DtiStudio, version 1.02, software (H. Jiang, S. Mori, Department of Radiology, Johns Hopkins University, Baltimore, Md) was used for tensor calculations (6,10). All source images from the DT imaging data sets were visually inspected by one author (T.O.), and images with visually apparent artifacts due to bulk motion were removed. In our DT imaging data set, there was low eddy current–related

Radiology 2006; 238:668–678

Abbreviations:
DT = diffusion tensor
ROI = region of interest

Author contributions:
Guarantors of integrity of entire study, T.O., Y.M., K.T.; study concepts/study design or data acquisition or data analysis/interpretation, all authors; manuscript drafting or manuscript revision for important intellectual content, all authors; approval of final version of submitted manuscript, all authors; literature research, T.O., Y.M., Y.F., H.F., M.H., K.T.; clinical studies, T.O., Y.M., Y.F., T.H., M.K., A.Y., S.U., K.T.; statistical analysis, T.O., Y.M., M.K., A.Y., M.H., K.T.; and manuscript editing, all authors

Address correspondence to Y.M.
(e-mail: *mikiy@kuhp.kyoto-u.ac.jp*).

Authors stated no financial relationship to disclose.

geometric distortion between images obtained in each motion-probing gradient direction (23,25), so postprocessing distortion correction was not applied for this data set. After calculating the six independent elements of the 3 × 3 tensor and diagonalization, three eigenvalues and three eigenvectors were obtained (1,3–5). The eigenvector associated with the largest eigenvalue was assumed to represent the intravoxel fiber orientation. The fractional anisotropy map and directional color-coded map were synthesized (Fig 1). Fiber orientations were assigned specific colors on the color-coded map, as follows: Red represented the right-to-left orientation; green, the anterior-to-posterior orientation; and blue, the superior-to-inferior orientation (26).

Fiber Tractography

The DtiStudio software was used to also perform fiber tractography on the basis of the fiber assignments derived by means of the continuous tracking method (6,9,10). With this software, tracking from all the pixels inside the brain (ie, with the brute force approach) was performed, and tracking results that penetrated the two manually segmented regions of interest (ROIs) on the basis of the known anatomic distributions of tracts were assigned to specific tracts (ie, with the two-ROI approach). Propagation in each fiber tract was terminated if a voxel with a fractional anisotropy value of less than 0.2 was reached or if the inner product of two consecutive vectors was greater than 0.75. These conditions prohibited the turning of angles larger than 41° during tracking (10).

Four fiber bundles—the corticospinal tract, the superior longitudinal fasciculus, the corticocortical connection fibers through the corpus callosum, and the limbic fibers through the fornix—were reconstructed by drawing specific ROIs according to the anatomic distributions of each fiber tract. ROI manipulations were performed by one neuroradiologist (A.Y.) with 3 years of experience performing tractography and 10 years of experience as a neuroradiologist. This author was blinded as to whether the images had been obtained by using 3.0 T or 1.5 T when he performed each ROI segmentation.

For corticospinal tract tractography, two ROIs were placed on transverse non–diffusion-weighted ($b = 0$ sec/mm^2) images (10,12,15) according to established anatomic landmarks: The first ROI was placed in the cerebral peduncle bilaterally, and the second ROI was placed in the precentral gyrus bilaterally (27) (Fig 2a).

The superior longitudinal fasciculus was reconstructed at tractography by placing two ROIs in the cerebral deep white matter on a coronal directional color-coded map. The superior longitudinal fasciculus was identified on the coronal color-coded map as a region where the fiber orientation was anterior to posterior (green), lateral to the corona radiata (26,28). An anterior ROI was placed in the plane passing through the reconstructed corticospinal tract, and a posterior ROI was placed in the plane passing through the rostral surface of the splenium of the corpus callosum, with both ROIs covering the green area representing the superior longitudinal fasciculus (Fig 2c). Some "noise" fibers that were apparently tracing the error course were then removed (10).

Corpus callosum tractography was performed by imaging the combination of four different callosal fiber bundles. The primary ROI was placed in the corpus callosum in the midsagittal plane (Fig 2d). To visualize different parts of the callosal fibers, secondary ROIs were placed in four regions: two ROIs on the coronal color-coded map and two ROIs on the transverse color-coded map (Fig 2e). Anterior callosal fibers, referred to as minor forceps, were reconstructed by placing the ROI covering the deep white matter in the coronal plane anterior to the genu of the corpus callosum. For reconstruction of the posterior cal-

Figure 1

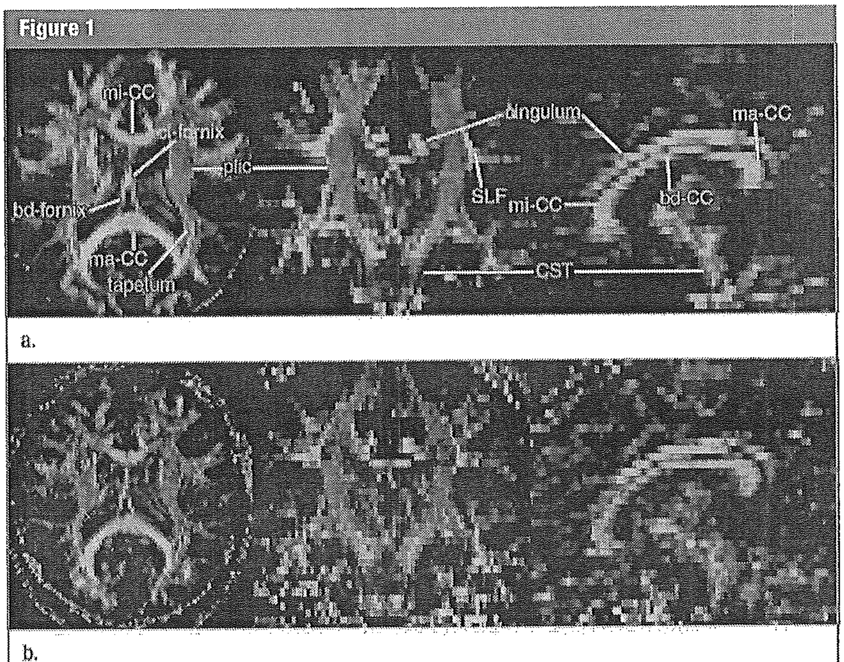

Figure 1: Transverse (left), coronal (middle), and sagittal (right) **(a)** 3.0-T and **(b)** 1.5-T color-coded maps reconstructed at DT tractography in the same subject. Red, green, and blue areas represent fibers running in right-to-left, anterior-to-posterior, and superior-to-inferior orientations, respectively. Locations of examined white matter tracts were assigned by using the 3.0-T color-coded maps. *bd-CC* = body of corpus callosum, *bd-fornix* = body of fornix, *cl-fornix* = column of fornix, *CST* = corticospinal tract, *ma-CC* = major forceps, *mi-CC* = minor forceps, *plic* = posterior limb of internal capsule (including the corticospinal tract), *SLF* = superior longitudinal fasciculus.

Figure 2

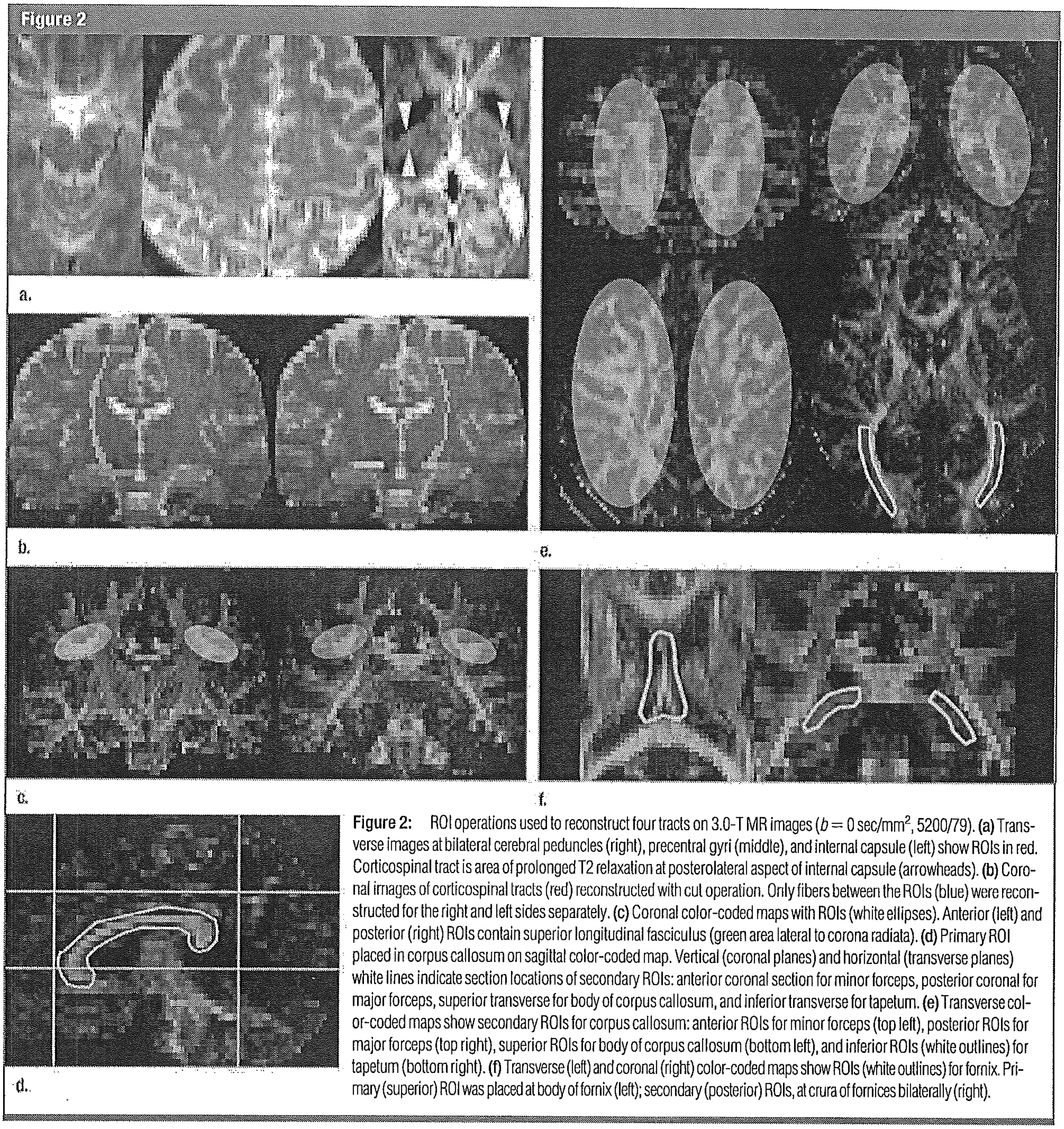

Figure 2: ROI operations used to reconstruct four tracts on 3.0-T MR images ($b = 0$ sec/mm^2, 5200/79). **(a)** Transverse images at bilateral cerebral peduncles (right), precentral gyri (middle), and internal capsule (left) show ROIs in red. Corticospinal tract is area of prolonged T2 relaxation at posterolateral aspect of internal capsule (arrowheads). **(b)** Coronal images of corticospinal tracts (red) reconstructed with cut operation. Only fibers between the ROIs (blue) were reconstructed for the right and left sides separately. **(c)** Coronal color-coded maps with ROIs (white ellipses). Anterior (left) and posterior (right) ROIs contain superior longitudinal fasciculus (green area lateral to corona radiata). **(d)** Primary ROI placed in corpus callosum on sagittal color-coded map. Vertical (coronal planes) and horizontal (transverse planes) white lines indicate section locations of secondary ROIs: anterior coronal section for minor forceps, posterior coronal for major forceps, superior transverse for body of corpus callosum, and inferior transverse for tapetum. **(e)** Transverse color-coded maps show secondary ROIs for corpus callosum: anterior ROIs for minor forceps (top left), posterior ROIs for major forceps (top right), superior ROIs for body of corpus callosum (bottom left), and inferior ROIs (white outlines) for tapetum (bottom right). **(f)** Transverse (left) and coronal (right) color-coded maps show ROIs (white outlines) for fornix. Primary (superior) ROI was placed at body of fornix (left); secondary (posterior) ROIs, at crura of fornices bilaterally (right).

losal fibers, referred to as major forceps, the ROI was placed posterior to the splenium of the corpus callosum. Callosal body fibers were reconstructed by placing the ROI at the centrum semiovale in the transverse plane superior to the body of the corpus callosum. For reconstruction of the temporal interhemispheric connection fibers, referred to as tapetum, ROIs were placed bilaterally in the temporal deep white matter, lateral to the trigon of the lateral ventricles. These four fibers (ie, minor forceps, major forceps, callosal body fibers, and tapetum) were combined to delineate the entire corpus callosum.

Limbic fibers through the fornix were reconstructed by placing one primary ROI and two secondary ROIs. The primary ROI was placed in the body of the fornix, and the secondary ROIs

Figure 3

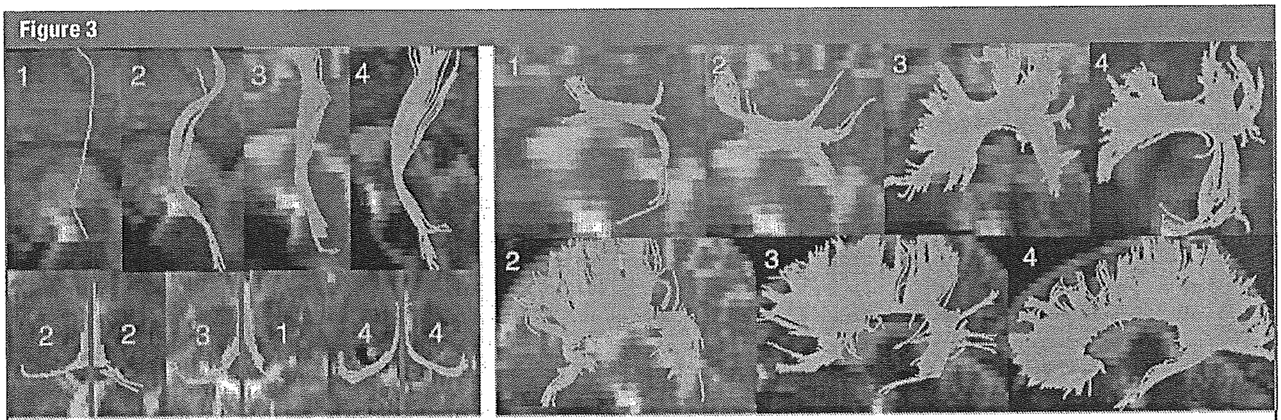

a. b.

Figure 3: Scoring (scores *1–4*) for fiber tract depiction at tractography. Red areas represent the depicted tracts. **(a)** Top: Corticospinal tractographic image superimposed on sagittal non–diffusion-weighted images (5200/79) viewed from left side. Grades *1* and *2* were assigned at 1.5-T imaging, and grades *3* and *4* were assigned at 3.0-T imaging. Bottom: Fornix tractographic image obtained at 3.0 T superimposed on transverse non–diffusion-weighted images (5200/79). Blue lines separate right and left fornix tractographic images. **(b)** Superior longitudinal fasciculus tractographic image (top) and corpus callosum tractographic image (bottom) superimposed on sagittal non–diffusion-weighted images (5200/79) viewed from left side. For superior longitudinal fasciculus tractography (top), grades 1 and 2 were assigned at 1.5-T imaging, and grades 3 and 4 were assigned at 3.0-T imaging. For corpus callosum tractography, grade 2 was assigned at 1.5 T imaging, and grades 3 and 4 were assigned at 3.0-T imaging. In no subject was grade 1 assigned at corpus callosum tractography.

were placed in the crura of the right and left fornices anterolateral to the splenium of the corpus callosum (Fig 2f).

Evaluation of Tractography

The tractographic depiction of fiber tracts was graded on three-dimensional volume views and in three orthogonal two-dimensional planes by two neuroradiologists (T.O., with 2 years of experience performing tractography; Y.M., with 3 years of experience performing tractography and 19 years of experience as a neuroradiologist). Grading was performed on the basis of the following three criteria: the fiber tract volume, the anatomic distribution of the tract, and the presence or absence of the tract at the expected location. The readers were blinded to the magnetic field strength used (1.5 or 3.0 T). After performing independent interpretations, the two readers resolved any score discrepancies by consensus to establish final scores.

One score was derived from one tractographic examination—not from the pair of ROIs used to perform reconstructing tractography. The scores assigned at fiber tractography were as follows: 4 meant excellent—that is, the depicted fiber tract accurately matched the known anatomic distribution, and there was a sufficient volume of fibers; 3 meant adequate for diagnosis—that is, imaging errors such as image distortion and tract propagation error were minor, so the image was still adequate for use as a diagnostic tool; 2 meant fair—that is, moderate imaging errors or moderate tract volume loss markedly reduced imaging quality; 1 meant poor—that is, there were major imaging errors and/or tract volume loss, and the readers were unable to interpret the course or shape of the tract; and 0 meant no tract visualization.

At corticospinal tract tractography, anatomically accurately depicted tracts were defined as those passing through the lateral segment of the cerebral peduncle, the posterior limb of the internal capsule, and the precentral gyrus. At superior longitudinal fasciculus tractography, fibers connecting the frontal and parietal lobes (ie, long association fibers) and fibers connecting the frontal and temporal lobes (ie, arcuate fibers) were considered. Anatomically accurate results for the superior longitudinal fasciculus were defined as good visualization of both the long association fibers and the arcuate fibers. At corpus callosum tractography, anatomically accurate results were defined as good visualization of the four different subsegments. At limbic tractography, the depiction of fibers connecting the column, body, and crus of the fornix was considered to represent anatomically accurate results. At tractography, the depicted superior longitudinal fasciculus, corpus callosum, and fornix are each composed of several subsegments of fiber bundles, and all subsegments were integrated to establish a single final score for each tractographic examination. The scoring of tractographic images is illustrated in Figure 3.

Tractographic depictions of the corticospinal tract, superior longitudinal fasciculus, and fornix on the right and left sides were assessed independently. At corpus callosum tractography, the right and left sides were assessed together, because callosal fiber connects the right and left hemispheres.

Reconstructed tract fibers were counted by using the DtiStudio software. The numbers of fibers depicted at tractography of the corticospinal tract and the superior longitudinal fasciculus in the right and left hemispheres were counted separately. The right and left fibers were not counted separately at tractography of the corpus callosum and the fornix, because right- and left-hemisphere limbic fibers were difficult to differentiate at the column of the fornix, which was visualized as a single fiber bundle.

Although the diffusion characteristics of the normal brain are somewhat asymmetric, corticospinal tract tractography in healthy subjects reportedly reveals minimal asymmetry (17,29). To assess the reliability of corticospinal tract tractography in healthy subjects, lateral asymmetry was evaluated on the basis of the numbers of right- and left-hemisphere fibers at tractography of the corticospinal tract. For this purpose, the "cut" operation was performed by using DtiStudio software. With the cut operation, only the fiber coordinates between the two ROIs are reconstructed (Fig 2b). The conventional two-ROI approach involves the use of three corticospinal tract regions at tractography: the areas below the cerebral peduncle, between the two ROIs, and above the precentral gyrus. These three regions have very different properties. In the region between the two ROIs, tracking results do not branch and are more robust against noise. This approach is particularly useful for quantitative analysis.

The index of asymmetry (AI) between the right (*R*) and left (*L*) corticospinal tracts in each subject at tractography was calculated as the absolute difference in fiber numbers between the two sides, divided by the mean of the two sides, as modified from a previously described method (14): $AI = L - R / [(L + R)/2]$. Lateral asymmetry analysis of superior longitudinal fasciculus tractography was not performed, because the superior longitudinal fasciculus comprises numerous long and short connecting fibers and lateral asymmetry is commonly observed in healthy subjects (6,29).

Statistical Analyses

Differences between 3.0- and 1.5-T DT imaging were calculated in terms of the following features: *(a)* depiction scores for right and left corticospinal tract tractography, right and left superior longitudinal fasciculus tractography, corpus callosum tractography, and right and left fornix tractography; *(b)* numbers of fibers depicted at right and left tractography of the corticospinal tract, right and left tractography of the superior longitudinal fasciculus, corpus callosum tractography, and fornix tractography; and *(c)* asymmetry index at corticospinal tract tractography. Statistical

Figure 4

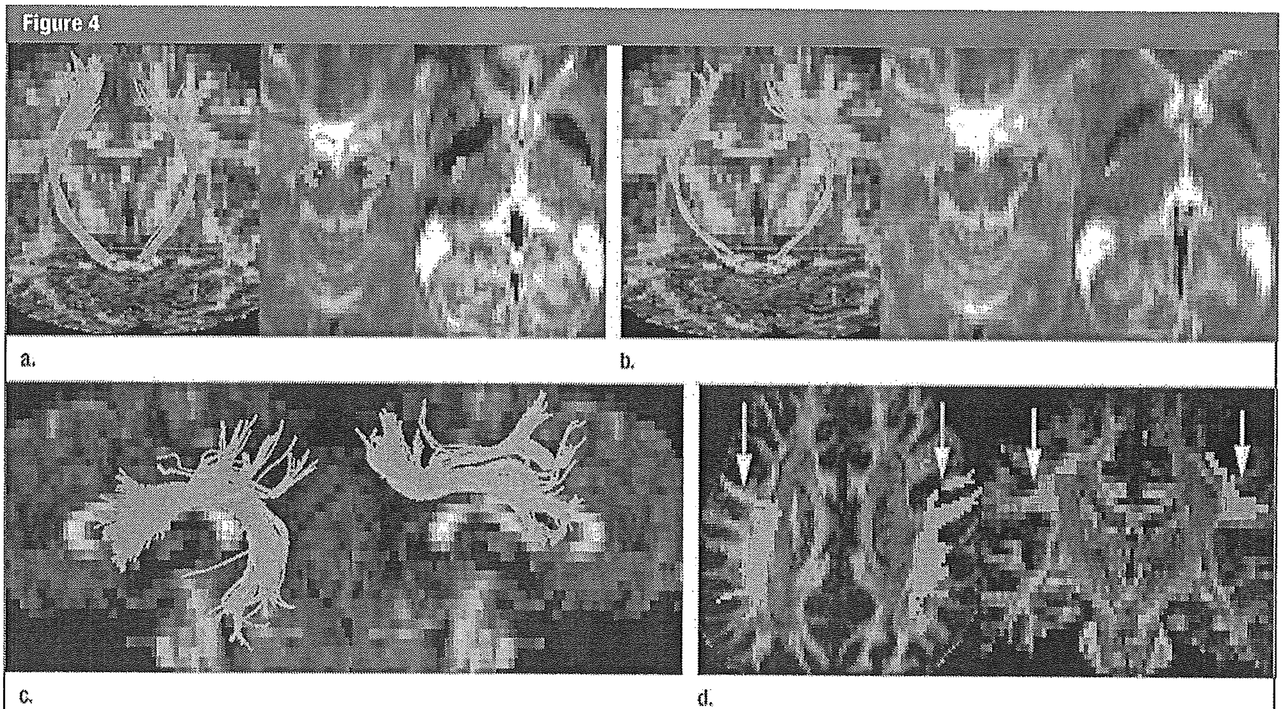

Figure 4: Fiber tractographic results. **(a, b)** Left: Three-dimensional reconstruction of corticospinal tract (red) in the same subject at **(a)** 3.0-T and **(b)** 1.5-T tractography, with use of transverse and coronal fractional anisotropy images. Middle and right: Transverse non–diffusion-weighted images with two-dimensional overlays of tractographic images at the sections of the cerebral peduncles (middle) and internal capsule (right) bilaterally. The voxels where the depicted corticospinal tract penetrates the transverse planes are shaded red. At 1.5-T corticospinal tract tractography (b), although the proper anatomic distribution is depicted, the tract volume is lower than that at 3.0 T. **(c)** Three-dimensional reconstruction of superior longitudinal fasciculus (red) on sagittal fractional anisotropy map at 3.0-T tractography in a different subject. At tractography in this subject, the shapes and distributions of the right and left superior longitudinal fasciculi differed. Although tractography of the left superior longitudinal fasciculus depicted arcuate fibers toward the temporal lobe, tractography of the right superior longitudinal fasciculus depicted no arcuate fibers. The cortico-cortical long connection fibers between the frontal and parietal lobes, however, were thicker on the right side than on the left side. **(d)** Tractographic image of superior longitudinal fasciculus (red, arrows) overlaid on 3.0-T transverse (left) and coronal (right) color-coded maps obtained in the subject described in c *(Fig 4 continues)*.

analysis was based on the consensus scores for each tract in each subject derived by the two neuroradiologists. The Wilcoxon signed rank test was applied by using JMP, version 5.1, software (SAS Institute, Cary, NC). For all statistical analyses, $P < .05$ was considered to be indicative of a significant difference.

Results

Fiber Tract Visualization

DT imaging at both 3.0 and 1.5 T was successfully performed in all 30 subjects. The corticospinal tract was visualized at 3.0 and 1.5 T (Fig 4a, 4b) in all subjects. At superior longitudinal fasciculus tractography, long association fibers were visualized in all subjects at 3.0 and 1.5 T. Right arcuate fibers were visualized in 22 subjects (73%) at 3.0 T and in 20 subjects (67%) at 1.5 T, whereas left arcuate fibers were identified in 29 subjects (97%) at 3.0 and 1.5 T (Fig 4c, 4d).

All four subsegments of the corpus callosum were successfully visualized at 3.0 and 1.5 T (Fig 4e) in every subject. The body and column of the fornix were visualized at 3.0 and 1.5 T in every subject. The right crus of the fornix was visualized in 21 subjects (70%) at 3.0 T and in 18 subjects (60%) at 1.5 T. The left crus of the fornix was visualized in 27 subjects (90%) at 3.0 T and in 25 subjects (83%) at 1.5 T (Fig 4f). One subject was incidentally found to have cavum septum pellucidum and cavum vergae. The right and left columns of the fornix were visualized separately in this subject (Fig 4g).

All tractographic results were included in the analysis of tract depiction scores and numbers of depicted tract fibers. All tractographic results for the corticospinal tract were included for asymmetry analysis. With regard to the 420 depiction scores (30 subjects times seven tracts times two readers), there were discrepancies between the two independent readers regarding 152 scores (36%). The two readers discussed the discrepancy and established a final consensus score in each case. The depicted fiber tracts and the depiction scores are listed in Table 1.

Statistical Analyses

For tractography of the corticospinal tract, both right- and left-hemisphere depiction scores ($P < .001$) and numbers of tract fibers (right, $P = .008$; left, $P < .001$) were significantly higher at 3.0 T than at 1.5 T. The asymmetry index at corticospinal tract tractography was significantly lower at 3 T ($P < .001$). For tractography of the right su-

Figure 4

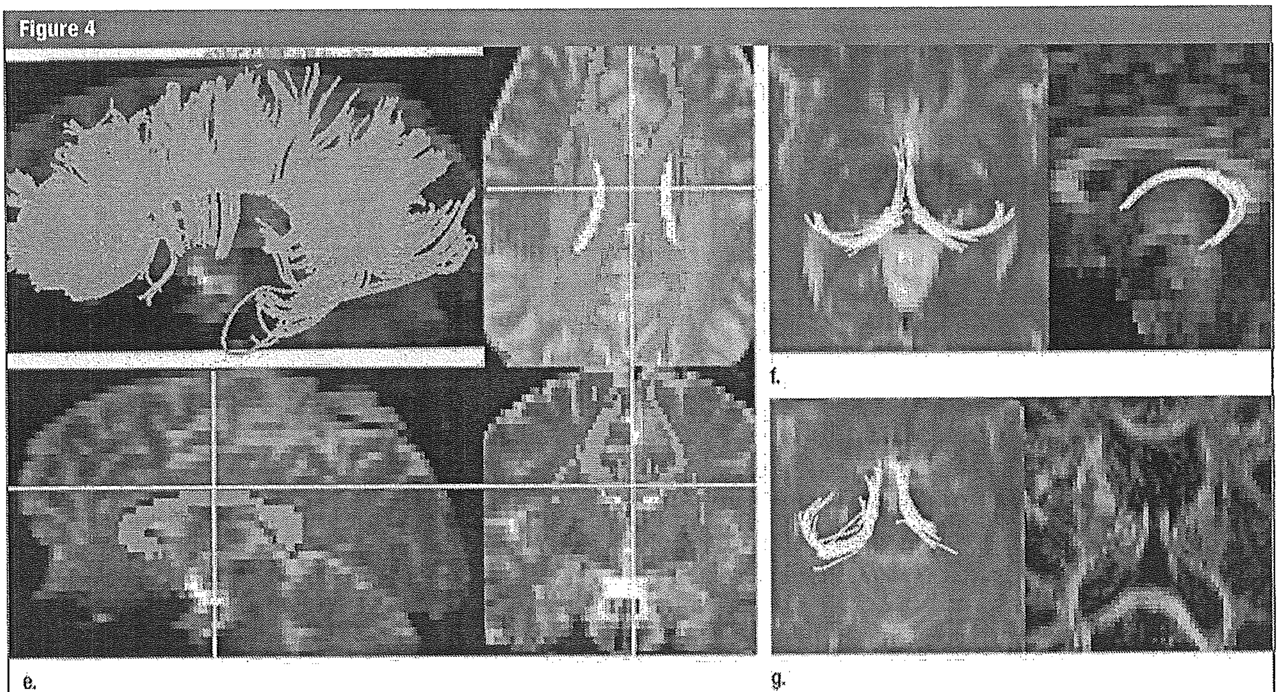

Figure 4 *(continued)*: **(e)** Three-dimensional 3.0-T tractographic reconstruction of corpus callosum (red) on sagittal non–diffusion-weighted image (5200/79) (top left) and on overlay in three orthogonal planes (top right, bottom left, and bottom right). Various kinds of transcallosal connection fibers are depicted. The center indicated by the intersecting of the vertical and horizontal lines on the three orthogonal images (top right, bottom left, and bottom right) indicate the same location. **(f)** Three-dimensional 3.0-T tractographic reconstruction of fornix (yellow) on transverse non–diffusion-weighted image (5200/79) (left) and sagittal color-coded map viewed from left (right). **(g)** Three-dimensional 3.0-T tractographic reconstruction of fornix (yellow) on transverse non–diffusion-weighted image (5200/79) (left) and transverse color-coded map (right) obtained in a subject with cavum septum pellucidum and cavum vergae. The bodies and columns of the fornices on the right and left sides were visualized separately.

perior longitudinal fasciculus, depiction scores ($P = .005$) and numbers of tract fibers ($P = .001$) were significantly higher at 3.0 T than at 1.5 T. Depiction scores for tractography of the left superior longitudinal fasciculus did not differ significantly between 3.0- and 1.5-T DT imaging. For tractography of the left superior longitudinal fasciculus, the numbers of tract fibers were significantly higher at 3.0 T than at 1.5 T ($P = .02$). For corpus callosum tractography, depiction scores were significantly higher at 3.0 T than at 1.5 T ($P = .01$), although the numbers of tract fibers did not differ significantly. Scores for depiction of the right fornix ($P = .04$) and numbers of fornix tract fibers bilaterally ($P = .02$) were significantly higher at 3.0 T than at 1.5 T, although scores for depiction of the left fornix were not significantly different. These results are summarized in Table 2.

Table 1

Depiction Scores Assigned at Fiber Tractography

Tract and Score	3.0-T Tractography	1.5-T Tractography
Right corticospinal tract		
0	0	0
1	0	2
2	1	8
3	6	13
4	23	7
Left corticospinal tract		
0	0	0
1	0	6
2	1	9
3	6	10
4	23	5
Right superior longitudinal fasciculus		
0	0	0
1	1	3
2	10	11
3	6	9
4	13	7
Left superior longitudinal fasciculus		
0	0	0
1	1	0
2	3	3
3	14	17
4	12	10
Corpus callosum		
0	0	0
1	0	0
2	2	6
3	9	14
4	19	10
Right fornix		
0	0	0
1	10	11
2	8	16
3	11	3
4	1	0
Left fornix		
0	0	0
1	3	4
2	14	17
3	12	9
4	1	0

Note.—Data are numbers of subjects with the given depiction score. Scores were determined in consensus between two readers.

Discussion

In recent studies, investigators have reported on intraindividual comparisons between 3.0- and 1.5-T DT imaging performed for functional MR imaging based on blood oxygen level–dependent contrast (30), intracranial time-of-flight MR angiography (31), supraaortic contrast material–enhanced MR angiography (32), and high-spatial-resolution inner ear imaging (33). These studies revealed the clinical feasibility of and the better visualization that is achievable at 3.0-T imaging compared with these features at 1.5-T imaging. DT imaging also reportedly yields a higher signal-to-noise ratio at 3.0 T, suggesting the possibility that it renders higher spatial resolution without enhanced noise-related errors (22,34).

Parallel imaging techniques involve the use of multiple receiver coil elements for spatial information encoding and gradient encoding and, owing to shortened echo train lengths, have been shown to markedly reduce the number of echo-planar imaging–related artifacts. The potential of parallel imaging for DT imaging has been demonstrated at both 1.5 and 3.0 T (21,22). Naganawa et al (23) challenged the optimization of 3.0-T DT fiber tractography performed with parallel imaging and found that DT imaging data on brain fiber tracking in healthy subjects can be acquired within a very short imaging time (<2 minutes). Nagae-Poetscher et al (24) performed high-spatial-resolution DT imaging of the brainstem at 3.0 T with parallel imaging and visualized various brainstem structures, including deep cerebellar nuclei, some cranial nerves, and white matter tracts.

To our knowledge, our study is the first in which the findings of 3.0- and

1.5-T DT fiber tractography, both performed with parallel imaging, were compared in a relatively large number of subjects. Improved image quality was observed at 3.0-T tractography of the corticospinal tract.

More complex results were observed at tractography of the superior longitudinal fasciculus. Although the right superior longitudinal fasciculus was visualized significantly better at 3.0 T, the depiction score for left superior longitudinal fasciculus tractography did not differ significantly between 3.0 and 1.5 T. The numbers of tract fibers depicted at 3.0 T were significantly higher than the numbers of fibers depicted at 1.0 T. We speculated that the reason for this was as follows: According to fiber dissection study findings, the corticospinal tract is a long projection fiber bundle with a well-established anatomic distribution (35). Most fibers in the corticospinal tract run parallel through the posterior limb of the internal capsule, without sharp turning angles or directional diversity.

Conversely, both the superior longitudinal fasciculus and the corpus callosum consist of groups of fiber bundles that comprise association or commissural fibers of varying lengths and directions. The superior longitudinal fasciculus contains arcuate fibers that turn sharply toward the temporal lobe. This sharp turning angle may surpass the tracking terminate threshold, and tracking does not extend to reach the temporal lobe. Temporal fibers are susceptible to image distortion at the middle cranial fossa and temporal bone, where the air-tissue interface induces magnet susceptibility artifacts. Thus, we propose that temporal arcuate fibers are more affected by image distortion than are long association fibers. In the present study, left arcuate fibers were visualized in a larger number of subjects than were right arcuate fibers at both 3.0 and 1.5 T. Such asymmetry of the arcuate fibers at tractography may be due to image distortion or the known lateral asymmetry of temporal fibers (36), and, thus, differences between 3.0- and 1.5-T DT imaging may be underestimated on the left side.

Table 2

Analyses of Tract Depiction Scores and Numbers of Tract Fibers

Tract	Difference in Depiction Score*	*P* Value[†]	Difference in No. of Tract Fibers*	*P* Value[‡]
Right corticospinal tract[§]	0.87 ± 0.15	<.001	27 ± 12	.008
Left corticospinal tract	1.32 ± 0.21	<.001	70 ± 9.2	<.001
Right superior longitudinal fasciculus	0.52 ± 0.16	.005	192 ± 57	.001
Left superior longitudinal fasciculus	0.03 ± 0.14	NS	65 ± 34	.02
Corpus callosum	0.34 ± 0.12	.01	220 ± 149	NS
Right fornix	0.35 ± 0.16	.04	...	...
Left fornix	0.19 ± 0.15	NS	...	...
Left and right fornices	...	...	14 ± 5.5	.02

Note.—NS = not significant.

* Data are mean difference values ± standard deviations.

[†] *P* values for difference in depiction scores at 1.5- versus 3.0-T tractography.

[‡] *P* values for difference in numbers of tract fibers at 1.5- versus 3.0-T tractography.

[§] The mean asymmetry index for the corticospinal tract was 0.47 ± 0.11 (standard deviation), and the difference in corticospinal tract asymmetry index at 1.5- versus 3.0-T tractography was significant ($P < .001$).

For corpus callosum tractography, tract depiction scores were better at 3.0 T than at 1.5 T but the numbers of tract fibers did not differ significantly. At corpus callosum tractography, the crossing-fiber problem of unidirectional tracking models (37) may contribute to the discrepancies observed between depiction scores and tract fiber numbers. Corpus callosum tractography is susceptible to the crossing-fiber problem at the centrum semiovale. In this area, a small number of callosal fibers intersect a large number of corticospinal tract fibers. Thus, corpus callosum tractography might reveal a smaller number of fibers than the appropriate fiber trajectory owing to limitations related to the crossing-fiber problem, and differences between 3.0- and 1.5-T imaging may be underestimated.

The statistical methods used may have been responsible for the differences in results obtained at analyses of the depiction scores and the numbers of tract fibers. Although mean differences in the numbers of depicted fibers between 3.0- and 1.5-T imaging were as large as 220, no significant difference was noted. This was probably because of the relatively large numbers of depicted fibers (mean numbers: 3784 at 3.0 T and 3565 at 1.5 T). Low statistical power also may have contributed to this lack of a significant difference.

Depiction scores for right fornix tractography were significantly better at 3.0 T than at 1.5 T, but no significant differences were noted for the left fornix. The numbers of tract fibers depicted at 3.0-T fornix tractography were significantly higher than the numbers depicted at 1.5-T tractography. This result was probably due to the relatively lower volume of limbic fibers compared with the volumes of other fiber bundles. Our DT imaging voxel size was 1.7 × 1.7 × 3.0 mm. The body and crus of the fornix are composed of narrow fiber bundles—they are smaller in diameter than a single voxel—so partial volume-averaging artifacts would have had a greater effect in this region than in the other fiber tracts.

The present study had some limitations. First, the imaging parameters for 3.0-T imaging were not optimized to achieve the best DT image quality. For the most part, we used identical imaging parameters to perform 3.0- and 1.5-T imaging for comparisons so that features other than magnetic field strength would be equivalent. However, differences in T1 and T2* interfere with the equal conditions between 3.0- and 1.5-T imaging. A DT imaging sequence optimized for 1.5-T imaging is not the optimal sequence for 3.0-T imaging. The differences in bandwidth between 3.0- and 1.5-T imaging also may have biased our results. We tried to keep other acquisition parameters equivalent between 3.0- and 1.5-T imaging, but the bandwidth was higher at 3.0 T. Higher bandwidth results in a reduced signal-to-noise ratio and reduced image distortion. DT imaging at 3.0 T yields a higher signal-to-noise ratio and causes greater magnet susceptibility artifacts owing to the higher static magnetic field strength. We adjusted parameters so that we could use a bandwidth of 1502 Hz per pixel for 3.0-T imaging, which is up to 50% higher than the bandwidth used for 1.5-T imaging. Further optimization of 3.0-T imaging to improve the quality of DT images may be required in the future.

Second, the development of imaging methods to reduce the effects of the crossing-fiber problem, such as high angular DT imaging with high *b* values (38) and diffusion-spectrum imaging (36), is progressing. Other fiber-tracking methods, such as probabilistic tractography to estimate the probability of fiber connections through the data field (39), also are advancing. These advanced methods will affect the results of both 3.0-T and 1.5-T tractography.

In conclusion, DT tractography at 3.0 T enables improved visualization of the corticospinal tract compared with DT tractography at 1.5 T, and 3.0-T tractography of the superior longitudinal fasciculus, corpus callosum, and fornix has some advantages over 1.5-T tractography. Advances in efficient MR sequences are needed to improve the image quality and reliability of 3.0-T DT tractography.

References

1. Basser PJ, Mattiello J, LeBihan D. MR diffusion tensor spectroscopy and imaging. Biophys J 1994;66:259-267.
2. Beaulieu C. The basis of anisotropic water diffusion in the nervous system: a technical review. NMR Biomed 2002;15:435-455.
3. Chenevert TL, Brunberg JA, Pipe JG. Anisotropic diffusion in human white matter: demonstration with MR techniques in vivo. Radiology 1990;177:401-405.
4. Pierpaoli C, Jezzard P, Basser PJ, Barnett A, Di Chiro G. Diffusion tensor MR imaging of the human brain. Radiology 1996;201:637-648.
5. Basser PJ, Pajevic S, Pierpaoli C, Duda J, Aldroubi A. In vivo fiber tractography using DT-MRI data. Magn Reson Med 2000;44:625-632.
6. Mori S, van Zijl PC. Fiber tracking: principles and strategies—a technical review. NMR Biomed 2002;15:468-480.
7. Masutani Y, Aoki S, Abe O, Hayashi N, Otomo K. MR diffusion tensor imaging: recent advance and new techniques for diffusion tensor visualization. Eur J Radiol 2003;46:53-66.
8. Dong Q, Welsh RC, Chenevert TL, et al. Clinical applications of diffusion tensor imaging. J Magn Reson Imaging 2004;19:6-18.
9. Stieltjes B, Kaufmann WE, van Zijl PC, et al. Diffusion tensor imaging and axonal tracking in the human brainstem. Neuroimage 2001;14:723-735.
10. Wakana S, Jiang H, Nagae-Poetscher LM, van Zijl PC, Mori S. Fiber tract–based atlas of human white matter anatomy. Radiology 2004;230:77-87.
11. Clark CA, Barrick TR, Murphy MM, Bell BA. White matter fiber tracking in patients with space-occupying lesions of the brain: a new technique for neurosurgical planning? Neuroimage 2003;20:1601-1608.
12. Yamada K, Kizu O, Mori S, et al. Brain fiber tracking with clinically feasible diffusion-tensor MR imaging: initial experience. Radiology 2003;227:295-301.
13. Huisman TA, Schwamm LH, Schaefer PW, et al. Diffusion tensor imaging as potential biomarker of white matter injury in diffuse axonal injury. AJNR Am J Neuroradiol 2004;25:370-376.
14. Glenn OA, Henry RG, Berman JI, et al. DTI-based three-dimensional tractography detects differences in the pyramidal tracts of infants and children with congenital hemiparesis. J Magn Reson Imaging 2003;18:641-648.
15. Kunimatsu A, Aoki S, Masutani Y, Abe O, Mori H, Ohtomo K. Three-dimensional white matter tractography by diffusion tensor imaging in ischaemic stroke involving the corticospinal tract. Neuroradiology 2003;45:532-535.
16. Tanenbaum LN. 3-T MR imaging: ready for clinical practice [letter]. AJNR Am J Neuroradiol 2004;25:1626-1627.
17. Zhai G, Lin W, Wilber KP, Gerig G, Gilmore JH. Comparisons of regional white matter diffusion in healthy neonates and adults performed with a 3.0-T head-only MR imaging unit. Radiology 2003;229:673-681.
18. Sodickson DK, Manning WJ. Simultaneous acquisition of spatial harmonics (SMASH): fast imaging with radiofrequency coil arrays. Magn Reson Med 1997;38:591-603.
19. Pruessmann KP, Weiger M, Scheidegger MB, Boesiger P. SENSE: sensitivity encoding for fast MRI. Magn Reson Med 1999;42:952-962.
20. Griswold MA, Jakob PM, Heidemann RM, et al. Generalized autocalibrating partially parallel acquisitions (GRAPPA). Magn Reson Med 2002;47:1202-1210.
21. van den Brink JS, Watanabe Y, Kuhl CK, et al. Implications of SENSE MR in routine clinical practice. Eur J Radiol 2003;46:3-27.
22. Jaermann T, Crelier G, Pruessmann KP, et al. SENSE-DTI at 3 T. Magn Reson Med 2004;51:230-236.
23. Naganawa S, Koshikawa T, Kawai H, et al. Optimization of diffusion-tensor MR imaging data acquisition parameters for brain fiber tracking using parallel imaging at 3 T. Eur Radiol 2004;14:234-238.
24. Nagae-Poetscher LM, Jiang H, Wakana S, Golay X, van Zijl PC, Mori S. High-resolution diffusion tensor imaging of the brain stem at 3 T. AJNR Am J Neuroradiol 2004;25:1325-1330.
25. Bastin ME, Armitage PA. On the use of water phantom images to calibrate and correct eddy current induced artefacts in MR diffusion tensor imaging. Magn Reson Imaging 2000;18:681-687.
26. Pajevic S, Pierpaoli C. Color schemes to represent the orientation of anisotropic tissues from diffusion tensor data: application to white matter fiber tract mapping in the human brain. Magn Reson Med 1999;42:526-540.
27. Naidich TP, Valavanis AG, Kubik S. Anatomic relationships along the low-middle convexity. I. Normal specimens and magnetic resonance imaging. Neurosurgery 1995;36:517-532.
28. Mori S, Kaufmann WE, Davatzikos C, et al. Imaging cortical association tracts in the human brain using diffusion-tensor-based axonal tracking. Magn Reson Med 2002;47:215-223.
29. Lazar M, Field AS, Lee J, et al. Lateral asymmetry of superior longitudinal fasciculus: a white matter tractography study (abstr). In: Proceedings of the 12th Meeting of the International Society for Magnetic Resonance in Medicine. Berkeley, Calif: International Society for Magnetic Resonance in Medicine, 2004; 1290.

30. Fera F, Yongbi MN, van Gelderen P, Frank JA, Mattay VS, Duyn JH. EPI-BOLD fMRI of human motor cortex at 1.5 T and 3.0 T: sensitivity dependence on echo time and acquisition bandwidth. J Magn Reson Imaging 2004;19:19–26.
31. Willinek WA, Born M, Simon B, et al. Time-of-flight MR angiography: comparison of 3.0-T imaging and 1.5-T imaging—initial experience. Radiology 2003;229:913–920.
32. Willinek WA GJ, von Falkenhausen M, et al. 3.0T contrast-enhanced, submillimeter MRA of the supraaortic arteries: does the signal gain at high field strength allow to replace the phased array coil by the quadrature body coil? (abstr). In: Proceedings of the 12th Meeting of the International Society for Magnetic Resonance in Medicine. Berkeley, Calif: International Society for Magnetic Resonance in Medicine, 2004; 1523.
33. Graf H, Schick F, Claussen CD, Seemann MD. MR visualization of the inner ear structures: comparison of 1.5 Tesla and 3 Tesla images. Rofo 2004;176:17–20.
34. Hunsche S, Moseley ME, Stoeter P, Hedehus M. Diffusion-tensor MR imaging at 1.5 and 3.0 T: initial observations. Radiology 2001; 221:550–556.
35. Yagishita A, Nakano I, Oda M, Hirano A. Location of the corticospinal tract in the internal capsule at MR imaging. Radiology 1994;191:455–460.
36. Lin CP, Wedeen VJ, Chen JH, Yao C, Tseng WY. Validation of diffusion spectrum magnetic resonance imaging with manganese-enhanced rat optic tracts and ex vivo phantoms. Neuroimage 2003;19:482–495.
37. Wiegell MR, Larsson HB, Wedeen VJ. Fiber crossing in human brain depicted with diffusion tensor MR imaging. Radiology 2000; 217:897–903.
38. Tuch DS, Reese TG, Wiegell MR, Makris N, Belliveau JW, Wedeen VJ. High angular resolution diffusion imaging reveals intravoxel white matter fiber heterogeneity. Magn Reson Med 2002;48:577–582.
39. Behrens TE, Woolrich MW, Jenkinson M, et al. Characterization and propagation of uncertainty in diffusion-weighted MR imaging. Magn Reson Med 2003;50:1077–1088.

INSTITUTE OF PHYSICS PUBLISHING PHYSICS IN MEDICINE AND BIOLOGY

Phys. Med. Biol. **50** (2005) 477–490 doi:10.1088/0031-9155/50/3/006

How much margin reduction is possible through gating or breath hold?

M Engelsman[1], G C Sharp[1], T Bortfeld[1], R Onimaru[2] and H Shirato[2]

[1] Department of Radiation Oncology, Massachusetts General Hospital, Harvard Medical School, 55 Fruit Street, Boston MA 02114, USA
[2] Department of Radiology, Hokkaido University School of Medicine, North-15 West-7 Kita-ku, Sapporo 060-8638, Japan

E-mail: mengelsman@partners.org

Received 29 September 2004, in final form 25 November 2004
Published 12 January 2005
Online at stacks.iop.org/PMB/50/477

Abstract

We determined the relationship between intra-fractional breathing motion and safety margins, using daily real-time tumour tracking data of 40 patients (43 tumour locations), treated with radiosurgery at Hokkaido University. We limited our study to the dose-blurring effect of intra-fractional breathing motion, and did not consider differences in positioning accuracy or systematic errors. The additional shift in the prescribed isodose level (e.g. 95%) was determined by convolving a one-dimensional dose profile, having a dose gradient representing an 8 MV beam through either lung or water, with the probability density function (PDF) of breathing. This additional shift is a measure for the additional margin that should be applied in order to maintain the same probability of tumour control as without intra-fractional breathing. We show that the required safety margin is a nonlinear function of the peak-to-peak breathing motion. Only a small reduction in the shift of isodose curves was observed for breathing motion up to 10 mm. For larger motion, 20 or 30 mm, control of patient breathing during irradiation, using either gating or breath hold, can allow a substantial reduction in safety margins of about 7 or 12 mm depending on the dose gradient prior to blurring. Clinically relevant random setup uncertainties, which also have a blurring effect on the dose distribution, have only a small effect on the margin needed for intra-fractional breathing motion. Because of the one-dimensional nature of our analysis, the resulting margins are mainly applicable in the superior–inferior direction. Most measured breathing PDFs were not consistent with the PDF of a simple parametric curve such as $\cos^4$, either because of irregular breathing or base-line shifts. Instead, our analysis shows that breathing motion can be modelled as Gaussian with a standard deviation of about 0.4 times the peak-to-peak breathing motion.

0031-9155/05/030477+14$30.00